Convection near threshold for Prandtl numbers near 1

Yuchou Hu,[1,2] Robert Ecke,[1] and Guenter Ahlers[1,2]
[1]*Center for Nonlinear Studies and Physics Division, Los Alamos National Laboratory, Los Alamos, New Mexico 87545*
[2]*Department of Physics and Center for Nonlinear Sciences, University of California, Santa Barbara, California 93106*
(Received 16 August 1993)

Rayleigh-Bénard convection in two cylindrical geometries with different sidewalls and with radius-to-height ratios $\Gamma=41$ and 43 was studied with shadowgraph imaging and heat-transport measurements. The working fluid was CO_2 at 25.3 bar with a Prandtl number $\sigma=0.93$. For one of the cells ($\Gamma=43$), axisymmetric convection rolls were stable above onset up to $\epsilon\equiv\Delta T/\Delta T_c-1=0.19$, where ΔT_c is the critical temperature difference. The amplitude of the center of the concentric patterns, the umbilicus, much larger near onset than that of the outlying region, grew as ϵ^{β_1}, with $\beta_1=0.27\pm0.04$. Outside the umbilicus, the amplitude grew as ϵ^{β_2}, with $\beta_2=0.48\pm0.04$. For $\Gamma=41$, axisymmetric convection rolls, coexisting with an annular cross-roll state confined near the sidewall, were the preferred patterns above onset and remained stable up to an ϵ of 0.08. The umbilicus of the concentric convection pattern shifted slightly off center as ϵ was increased, but the shift never exceeded 50% of the cell depth. For $\epsilon>0.10$, the patterns were unstable and evolved over many horizontal thermal diffusion times to straight-roll patterns with defects and grain boundaries. The process involved the umbilicus moving toward the sidewall, accompanied by radially traveling waves emitted by the umbilicus. While the umbilicus emitted, the crossrolls adjacent to the sidewall traveled parallel to the wall, and rolls were created and destroyed at a source and sink, respectively, presumably owing to large-scale flows generated by the off-centered position of the umbilicus.

PACS number(s): 47.20.−k, 47.27.−i, 47.54.+r

I. INTRODUCTION

A thin quiescent horizontal layer of fluid heated from below becomes unstable when the temperature difference ΔT across it exceeds a critical value ΔT_c [1]. The flow field which evolves for $\Delta T>\Delta T_c$ is known as Rayleigh-Bénard convection (RBC) [2]. The pattern which is formed by the flow has become a model for the study of pattern formation and wave-number selection in dissipative nonlinear nonequilibrium systems [3]. Even laterally large systems can display a variety of simple patterns of high symmetry such as straight rolls [4], concentric rolls [4–6], or hexagons [7,8], as well as more complicated textured patterns [4,6,9] which can incorporate different defect structures. The lateral boundary conditions are found to play a crucial role in determining the selected pattern, particularly when the system is close to the onset of convection. The tendency for rolls near a sidewall to be oriented perpendicular to that wall competes with the forces that prefer straight rolls far from boundaries [6,9–11]. For example, in cylindrical convection cells with a large radius-to-height ratio, two grain boundaries often separate the dominant straight-roll pattern from small regions of perpendicular rolls near the sidewall. The details of how a pattern will respond to the sidewalls seems to depend upon the Prandtl number σ, which is the ratio of the kinematic viscosity ν to the thermal diffusivity κ. In the present experiment we used CO_2 at a pressure of 25.3 bar as the fluid. It had $\sigma=0.93$. Another important parameter which influences the pattern is the lateral size, or aspect ratio Γ, of the system. The aspect ratio is defined as the ratio of the lateral extent to the layer height d. For a cylindrical cell, we take Γ to be the radius divided by d. For the work to be reported here, we have used two cylindrical cells with $\Gamma=41$ and 43. They differed primarily in the construction of the sidewalls.

When the convection cell is constructed of materials which lead to horizontal thermal gradients near the sidewalls, convection rolls tend to align with their axes parallel to these walls. This sidewall forcing can be either a transient which exists only when the temperature difference is being changed, or it can be static in nature [6,12,13]. Static forcing can be achieved deliberately by incorporating a heater in the wall [14] or by constructing part of the wall of highly conducting material [15], or unintentionally by nonuniform cooling of the top plate or incomplete thermal contact between the top or bottom plate and the sidewall [5]. To some extent it is present in all experimental cells. In the case of circular sidewalls, the forcing can lead to a concentric pattern [5]. If the static forcing is too weak, a concentric pattern may first form but then under steady conditions be unstable near onset [6]. Sufficiently strong static sidewall forcing will stabilize it [4,5,16]. Our cells had relatively weak sidewall forcing, with this forcing being somewhat stronger for the $\Gamma=43$ cell. We could also adjust the forcing somewhat by controlling the contact pressure between the walls and the top and bottom plates. With proper adjustment, we were able to create concentric rolls with minimal forcing.

In the remainder of this introduction we will discuss some of the interesting issues which arise in large-Γ systems with σ close to 1 and within 10% or so of the convective onset. We will mention briefly the relationship

between our experimental results and these issues. We will also briefly discuss previous works which are relevant.

The ability to create concentric roll patterns offers opportunities for the experimental investigation of interesting physical phenomena. One of these is the way in which the flow amplitude grows as ΔT increases beyond ΔT_c. In order to describe this, it is convenient to define the parameter $\epsilon = \Delta T / \Delta T_c - 1$, which is a dimensionless measure of the distance from the onset of convection. For small ϵ, convection under most conditions is well described by a Ginzburg-Landau equation [17–19] which applies to structures of straight or modestly curved rolls. For straight, uniform rolls, the amplitude is expected to grow as $\epsilon^{1/2}$ for small ϵ. This result has been verified quantitatively by experiment over a decade ago [20]. For axisymmetric patterns, the curved rolls away from the center are also expected to have an amplitude which grows as $\epsilon^{1/2}$. However, a problem arises in the treatment of the region near the center of the pattern where the theory at the level of the Ginzburg-Landau equation encounters a singularity and thus is not applicable [12,21]. A successful theoretical treatment of this problem was given by Pomeau, Zaleski, and Manneville [11] for large-aspect-ratio systems. The region near the umbilicus, the region next to the sidewall, and the region in between were treated separately with appropriate matching of the solutions at the interfaces between them. The authors predicted that for small ϵ the umbilicus amplitude would grow as $\epsilon^{1/4}$ provided that

$$\epsilon \gg 1/\Gamma^2 . \tag{1}$$

Since the theory is applicable only for small ϵ, and since Eq. (1) must be satisfied nonetheless, it is clear that a large-Γ system must be used for a quantitative comparison between experiment and theory. Earlier experimental observations using $\Gamma = 10$ showed that the amplitude of the umbilicus was larger than that of the outer regions and implied that the amplitude grew with an exponent less than $\frac{1}{2}$ [15]. A quantitative experimental investigation is difficult because the very forcing which stabilizes the state also makes the bifurcation imperfect, i.e., it produces "rounding" which distorts measurements near $\epsilon = 0$. In the experiment [15], the region next to the sidewall convected significantly at $\epsilon = -0.07$, and even the umbilicus had a noticeable amplitude well below the threshold of the unforced system. Thus a precise determination of the exponent was not possible. To study the predicted $\epsilon^{1/4}$ behavior of the umbilicus amplitude quantitatively while satisfying Eq. (1), one not only needs to study axisymmetric patterns in large-aspect-ratio containers, but the strength of the sidewall forcing also needs to be of a size which is just sufficient to stabilize the concentric states and yet small enough to cause minimal amplitude distortion near $\epsilon = 0$. We have been able to produce axisymmetric patterns in our cells with $\Gamma \simeq 40$ without the imposition of strong static sidewall forcing. This has enabled us to explore the axisymmetric state and its stability in the immediate vicinity of the convective onset without excessive rounding effects. In the present paper we will present quantitative measurements of the umbilicus amplitude which agree with the predictions of Pomeau, Zaleski, and Manneville [11]. Our results also illustrate the role of sidewall boundary conditions in determining the selected pattern at onset.

Stabilization of concentric patterns by static sidewall forcing offers other opportunities. Koschmieder and Pallas [5] as well as Croquette and Pocheau [16] employed it to study the stability and wave-number selection in these patterns for silicon oils with large values of σ and with $\Gamma \simeq 20$. They found that the patterns were time independent up to $\epsilon \simeq 5$ and that the wave number decreased in several steps as ϵ increased. An experiment using water with $\sigma = 6.1$ and $\Gamma = 7.5$ with very little static but some dynamic sidewall forcing was performed by Steinberg, Ahlers, and Cannell [6]. For $\epsilon < 0.16$, concentric patterns formed initially but were not stable. For $0.16 < \epsilon < 8$, however, concentric patterns were stable and time independent. These patterns also exhibited wave-number changes. The center of the concentric rolls, the umbilicus, shifted from the geometric center of the cell [6,16] before each wave-number change, merged with a roll *adjacent* to it, and then relaxed back to the cell center. In the process, the flow direction of the umbilicus was reversed. The net result was a reduction by one in the number of rolls in the system, i.e., a decrease in the wave number. Additional similar experiments using methanol with $\sigma \approx 7$ were done by Croquette, Le Gal, and Pocheau [22]. In all of these experiments, the Prandtl-number-dependent selected wave number was consistent with theoretical calculations [23–26].

Later experiments by Croquette [4] using argon with an even smaller $\sigma = 0.7$ and $\Gamma = 20$ showed a marked shrinkage in the range of time independence and a different instability mechanism. For $\epsilon = 0.18$ he found that time dependence set in by nucleation of dislocations *near the wall.* The formation of these dislocations was also associated with a shift of the umbilicus away from the center. After being formed, the dislocations glided towards the center where they successively converted the pattern into a spiral and then back again into concentric rolls. Nucleation of a new roll by the umbilicus led back to the original pattern, and the process repeated itself. Our results with $\Gamma \simeq 40$ and $\sigma \simeq 0.9$ likewise yielded a rather small range $\epsilon < 0.1$ for time-independent concentric rolls, but at least for one of our cells ($\Gamma = 41$) the mechanism by which the system became unstable was different. In the time-independent range $\epsilon < 0.1$ and for both cells, the wave number was essentially equal to its critical value. Over this small ϵ range and for our $\sigma = O(1)$, this is consistent with the theoretical prediction [23–26].

In our weakly forcing cell ($\Gamma = 41$) the pattern at small ϵ consisted of a narrow ring adjacent to the sidewall in which the roll axes were perpendicular to the wall (cross rolls). This ring had a width approximately equal to $4d$. It coexisted with concentric rolls which occupied the remainder of the cell. In the $\Gamma = 43$ cell, where the forcing was somewhat stronger, there were no cross rolls, and the pattern was composed entirely of concentric rolls. In the $\Gamma = 41$ cell, the umbilicus exhibited a small static shift at finite ϵ away from the geometric center which never

became larger than $\frac{1}{4}$ of a wavelength for $\epsilon < 0.08$. Time dependent patterns of *radially traveling waves* were observed for $\epsilon > 0.08$. This is qualitatively different from observations [4] with $\Gamma \simeq 20$, where (as described above) time dependence took the form of periodic defect-pair nucleations at the wall. The radially traveling wave emanated from the umbilicus, and the position of the umbilicus changed abruptly in the vicinity of the geometric cell center as the wave was emitted. For $0.08 \leq \epsilon \leq 0.10$, the waves provided a mechanism for the system to return temporarily to an essentially time-independent state of concentric rolls, because the emission of waves ceased when the umbilicus returned to the geometric center of the cell. For $\epsilon > 0.10$, the emitting umbilicus became unstable and moved from the center to the wall, thereby leading to the destruction of the concentric patterns. The resulting time-dependent patterns consisted of curved rolls terminating more or less orthogonal to the boundary. The patterns then also contained many defects.

An interesting feature of axisymmetric rolls related to the wave-number selection mechanism discussed in the previous paragraph is associated with the large-scale flows that can exist for finite Prandtl number [23,24,27]. A simple manifestation of these flows is the shift of the pattern center away from the geometric center of the cell which we discussed above [4,6,16,28]. Recent calculations [29] have yielded detailed predictions regarding the stability of the axisymmetric state with respect to off-center shifts. The ability to study these large-scale-flow effects presents an exciting opportunity for experimental investigations. With the cross rolls at the sidewall, we were able to probe the large-scale flow associated with off-centered axisymmetric patterns. When the radially traveling waves appeared, a source-sink pair of the cross rolls also appeared, with the source being roughly on the opposite side of the cell from the sink. The nucleation and destruction of the cross rolls caused traveling cross rolls which propagated parallel to the sidewall from the source to the sink. The wave-number distribution for the cross rolls showed that they were under a mean-flow stress [28] brought on by the large-scale flow for the off-centered concentric pattern.

The more strongly forced pattern with $\Gamma = 43$, which had no cross rolls near the wall, had different stability behavior. In this case, the umbilicus also shifted away from the center slightly, thereby compressing the rolls on the side of the cell towards which it had shifted. At $\epsilon = 0.19$, the compression led to the nucleation of a dislocation pair next to the wall. This is similar to the mechanism observed [4] for $\Gamma = 20$; however, the two defects climbed the concentric roll along the sidewall in opposite directions instead of gliding toward the umbilicus. The umbilicus then began to emit radially traveling waves, which in turn led to the formation of more defects near the wall. During this process, the umbilicus itself moved towards the wall, and after some time any remnant of the concentric pattern was destroyed.

After the concentric pattern had been destroyed in either cell, the resulting disordered pattern of curved rolls with many defects could be annealed at smaller ϵ and led to a near-perfect pattern of parallel rolls which were stable upon reducing ϵ until their amplitude vanished near $\epsilon = 0$. As had been found [4] for $\Gamma = 20$, there were, however, typically some cross rolls separated from the main area by two grain boundaries on opposite sides of the cell in the regions where a pure straight-roll pattern would be nearly parallel to the cell wall. Upon increasing ϵ again, these patterns become unstable in the same way as those for smaller Γ with argon [4,30]. Significant roll curvature, centered around the two grain boundaries on opposite sides of the cell, developed with increasing ϵ, and the rolls near the center of the cell become compressed. For $\epsilon > 0.1$ they were locally unstable via the skewed-varicose instability. A pair of dislocations then formed and moved away from the cell center towards the wall by a process involving a combination of climbing and gliding. For our larger Γ, however, several dislocations coexisted in the cell interior at all times, whereas for $\Gamma = 20$ the dislocations were able to reach the wall before a new nucleation of a pair would occur [4] in the cell center. An interesting question is whether this mechanism will continue to prevail as Γ is increased further. Preliminary measurements by Morris *et al.* [31] for a cell with $\Gamma = 78$ and for $\sigma = 0.9$ suggest that defect nucleation may occur at several places in the cell rather than only in the cell center.

In the next section we present a description of the experimental apparatus. The results of the amplitude and wave-number dependence on ϵ are presented in Sec. III. The stability of the concentric patterns, the interaction between concentric rolls and cross rolls, and the stability of straight rolls are discussed in Sec. IV. In Sec. V are further discussions and a brief summary of the findings.

II. EXPERIMENTAL SETUP

The apparatus is very similar to two others in use elsewhere [8,31]. A schematic diagram of the experimental setup is shown in Fig. 1. The cell bottom was a 6.4-mm-thick aluminum plate with mirror finish, and the top was

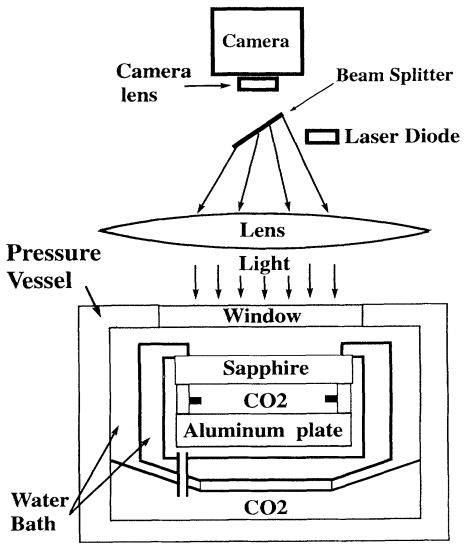

FIG. 1. Schematic diagram of the apparatus.

a 9.6-mm-thick optically flat sapphire window. The sapphire has a conductivity of about 0.37 W/(cm K), which exceeds that of the gas by a factor of about 2000. The conductivity of aluminum is an order of magnitude larger yet. Thus, for the purpose of heat-transport measurements, we have ignored the temperature variation across the thickness of both plates. The temperature of the bottom plate was measured with two thermistors embedded in it horizontally at midheight. A 92-Ω film heater was glued to the bottom side of the bottom plate to provide the heat current to drive convection. Two different circular sidewalls were used in the study, both made of three layers of 0.34-mm-thick cardboard paper. One had a spoiler tab [32,33] of thickness 0.34 mm at midheight extending 3.0 mm toward the center of the cell, while the other had no spoiler tab and thus a straight vertical edge. The conductivity of the paper is approximately 0.002 W/(cm K), which exceeds that of the gas by a factor of 10 and is smaller than that of the sapphire by a factor of 200. The sapphire window was held rigidly at its edge, and adjustments of its vertical position could be made independently of the sidewall at three points spaced about 120° apart. The uniformity of the cell height d was adjusted to within 0.002 mm by changing the sapphire position. The cell height could be changed by as much as 0.05 mm, thus changing the thermal attachment of the sidewall to provide adjustment of the static sidewall forcing. The drawback of this arrangement was the uncertainty in d, as we had no means to measure it directly after all adjustments were finished. However, it was determined indirectly through a comparison of ΔT_c with that of a calibration cell with a known cell height and through the assumption that at onset the wave number of the straight-roll structure was very close to the critical wave number, $q_c = 3.117$. For both sidewalls, d was determined to be 1.05 mm with an uncertainty of 1%. The sidewall with the spoiler tab had an aspect ratio $\Gamma \equiv (\text{radius})/d$ of 41, and Γ for the other sidewall was 43. The cells were filled with CO_2 at 25.3 bar with a Prandtl number of 0.93. The pressure was regulated by a temperature-controlled external ballast volume of gas. The pressure at the cell equilibrated with the ballast pressure extremely rapidly. The system pressure was regulated to within 0.005% by measuring it with a pressure transducer and by varying the ballast-volume temperature so as to minimize the deviations of the pressure-transducer readings from a setpoint. The variations of ΔT_c due to pressure variations were less than 0.01%. The time scale of the pattern dynamics is expected to be proportional to the vertical thermal diffusion time $\tau_v = d^2/\kappa$, where κ is the thermal diffusivity. For our cell we had $\tau_v = 3.2$ s. The cell was immersed in a circulating water bath whose temperature was measured by two thermistors placed near the water-pump outlet. The water temperature was controlled by heater wires placed between the water pump and the thermistors. The temperature regulation of the water bath yielded a temperature of the cell bottom of 33.702 °C on our temperature scale and with no heat input to the cell bottom. The cell-bottom temperature fluctuated slowly about a mean value by a few tenths of a milli-Kelvin. The mean temperature was steady for as long as a week within 0.2 mK.

The observation of the convection pattern was through the shadowgraph visualization method. A laser diode with a 45-μm aperture was used as a point light source. It was situated at the focal point of a telescope-quality lens. The light passing through the lens formed the parallel beam necessary for the imaging method. The addition of a camera lens before the charge-coupled-device (CCD) camera allowed control of both the image contrast and the image size. In the following sections, the processed shadowgraph images follow the convention that black regions correspond to hot fluid and white regions correspond to cold fluid. The processes simply involved dividing an image with convection by a background image taken in the conduction state. The image division took out distortions due to lighting nonuniformity and inhomogeneities of the cell-bottom reflectivity. For visual representations of the flow patterns, the divided images were rescaled so as to give good contrast. Quantitative determinations of amplitudes were based on the divided images, but of course without rescaling.

Finally, we mention here that the apparatus was located on a rotating table, thus enabling us to study the effect of a Coriolis force on the convection. However, the work reported in the present paper was done without rotation. As described below, we did use rotation to break up concentric patterns and thereby prepare straight-roll patterns when this was desired.

III. TIME-INDEPENDENT CONVECTION NEAR ONSET

A. Patterns near onset

Experiments in gases differ from experiments done in other fluids in an important respect: the relationship between the conductivity λ_w of the sidewall material and the conductivity λ_f of the fluid. Gases have such low conductivities that suitable sidewall materials have λ_w at least one order of magnitude greater than λ_f; by comparison, for liquids λ_w can be comparable to λ_f. A mismatch in the conductivities of the sidewall and the fluid can produce a horizontal temperature gradient near the wall if the top and/or bottom plates have a finite (albeit large) conductivity. This is so because the vertical heat currents through the wall and the fluid, and thus through those portions of the top (bottom) plate above (below) them, differ. This effect is one of the typical causes of static sidewall forcing [6]. It exists even when the wall makes good thermal contact with the top (bottom) plate. When this contact is poor, additional horizontal gradients will be induced in the fluid adjacent to the wall because then the wall will have a smaller vertical thermal gradient than the fluid near it. In our experiment, the cardboard sidewall material had a conductivity 10 times that of the gas and a factor of 200 less than that of the sapphire. In addition, the amount of heat conducted through the sidewall is about equal to that which passes through the gas layer. The consequent forcing was not sufficient to cause the patterns to have the cylindrical symmetry of the cell when the wall was compressed by

and thus thermally well attached to the top and bottom plate. An intentionally created gap of about 0.01 mm between the sidewall and the sapphire or bottom plate which was created by slightly increasing the cell spacing reduced the thermal contact and thus enhanced the horizontal gradients. It was required to generate and stabilize concentric patterns near the onset. However, this procedure did not always produce concentric patterns when the cell was taken apart and reassembled. This suggests that there are some uncontrolled variables, presumably involving the precise positioning of the wall relative to the sapphire and the bottom plate, which contributed to the sidewall forcing.

In order to gain some insight into the thermal sidewall forcing, we calculated the temperature fields in our cells near the wall assuming the fluid was at rest. The calculation was done by assuming constant-temperature boundary conditions at the top of the bottom plate (bottom of the fluid) and at the top of the sapphire. This is consistent with an effectively infinite bottom-plate conductivity and a large but finite conductivity of the sapphire. Shown in Fig. 2(a) is the temperature field created by the $\Gamma=43$ sidewall when it is thermally well-attached to the sapphire. The contour lines shown in the figure correspond to constant deviations of the temperature from the constant vertical temperature gradient which would exist

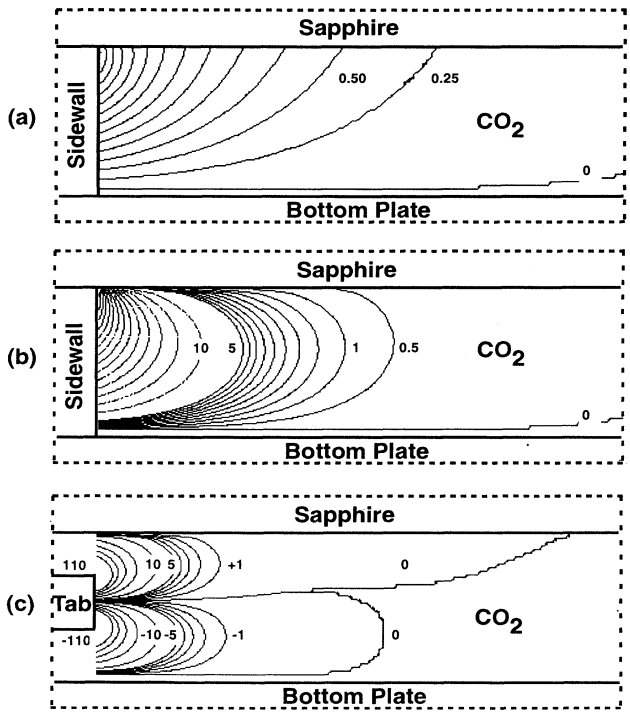

FIG. 2. Calculated deviations from a constant vertical temperature gradient near the sidewall. Portions of the sidewall, sapphire, cell bottom, and fluid layer are shown for (a) the $\Gamma=43$ wall in good contact with sapphire, (b) the $\Gamma=43$ wall used in the experiment, (c) the $\Gamma=41$ wall used in the experiment. The dimensions are to scale. The numbers indicated deviations from the linear profile of a horizontally infinite layer in 0.1%.

in the laterally infinite system without a sidewall. The numbers labeling the lines are the deviation, in units of 0.1%, of the total imposed temperature difference. For this straight-sidewall case with no gap, the horizontal temperature variation is about 0.3% and extends laterally about $2d$ into the fluid. For this case, the distortion of the temperature field is caused entirely by the temperature gradient in the sapphire, which is larger above the wall than it is above the fluid. Results of a calculation with a gap of 0.01 mm between the wall and the sapphire, which corresponds approximately to the experiment with $\Gamma=43$, are given in Fig. 2(b). They show that a substantial increase of the temperature distortion occurs near the gap. Instead of only 0.3%, the horizontal temperature variation is as large as 8%. The lateral range of the temperature inhomogeneity is comparable to that in Fig. 2(a). To reduce this lateral range, a spoiler tab [32,33] was added to the sidewall. The resulting temperature field is shown in Fig. 2(c). The temperature distortion near the gap is as big as before, but since the tab physically prevents convection in the region where the deviations are large, the deviations do not matter. The end of the tab defines the region over which the fluid can convect, and it is the distortion of the temperature field generated by the tab that is important. The deviation near the tab is around $\pm 11\%$, but this field is dipolelike and decreases rapidly away from the tab, reaching below 0.1% just $1d$ into the cell. This case corresponds approximately to our $\Gamma=41$ cell.

The strong forcing by the sidewall without a spoiler tab ($\Gamma=43$) produced concentric rolls at onset, as seen in Fig. 3(a). For the $\Gamma=41$ sidewall with a spoiler tab the patterns were also concentric rolls except for a narrow band of cross rolls next to the sidewall as seen in Fig. 3(b). The cross-roll region extended approximately from a radius of $37d$ to the wall at $41d$. Cross rolls adjacent to the sidewall in an otherwise concentric pattern have been observed previously, but so far as we know only as transients which after a long time led to a complete destruction of the concentric pattern [6,16]. In our cell, the state illustrated in Fig. 3(b) was stable. The cross-roll wavelength was 9% bigger than that of the concentric rolls near onset, and it decreased as ϵ was increased. For both types of time-independent concentric patterns, the wave number of the concentric rolls did not vary measurably with the radius but decreased very slightly with ϵ.

In addition to the concentric-roll patterns, straight-roll patterns could be produced by different procedures. One possible procedure consisted of applying a large amount of heat to the system in the conduction state, sufficient to bring it to $\epsilon \approx 1$; this produced a disordered time-dependent pattern full of defects and grain boundaries. Reducing the heat input until ϵ was near 0.08 would then permit the disordered pattern to heal to a time-independent straight-roll pattern [Fig. 3(c)]. This procedure could be extremely time consuming since the transients at the small ϵ sometimes lasted several days before they had decayed completely (on other occasions they might die out in half a day). Similar very long transients (much longer than horizontal thermal diffusion times which in our case were about 5000 s) have been observed

in previous experiments [6,9]. Alternatively, straight-roll patterns were obtained by utilizing the Küppers-Lortz (KL) instability [34]. The apparatus was rotated about a vertical axis with a sufficiently large rotation rate to allow the KL instability to break up the axisymmetric pattern. At rotation rates which were not too large, the coherent domains of straight rolls in the KL state were rather large, and after rotation was stopped, the transient which led to a pattern like the one in Fig. 3(c) was over in less than a day.

Measurements of the Nusselt number N for the parallel-roll state and the concentric patterns for $\Gamma=43$ are shown in Fig. 4. The Nusselt number is defined as the ratio of the effective conductivity of the fluid to the conductivity in the conduction state. Thus by definition it is equal to 1 in the conduction state. It increases linearly with ϵ for $0<\epsilon\ll 1$. The convective heat transport for the concentric-roll pattern and the straight-roll pattern was the same within experimental errors. Fitting N to a quadratic polynomial in ϵ (but omitting the points in the rounded region ($\epsilon<0.006$), we found $\Delta T_c=3.178\pm0.002$ °C. The rounding of N near ΔT_c was quite small, with N at ΔT_c equal to only about 1.002. Thus the sidewall forcing did not alter the bifurcation to convection very much near onset.

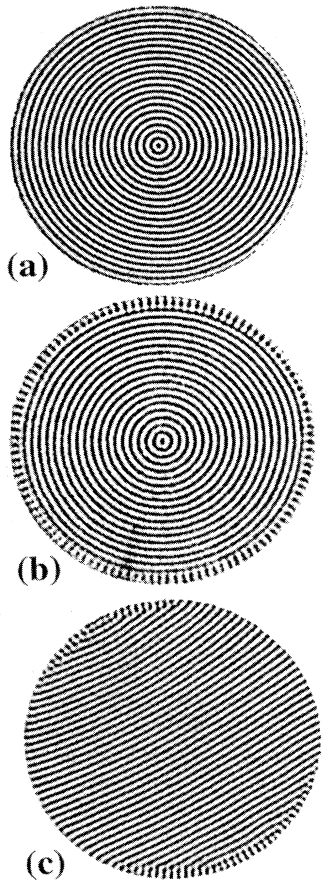

FIG. 3. Patterns at $\epsilon\approx0.04$. (a) Concentric-roll pattern for $\Gamma=43$; (b) cencentric-roll pattern for $\Gamma=41$; (c) straight-roll pattern for $\Gamma=43$.

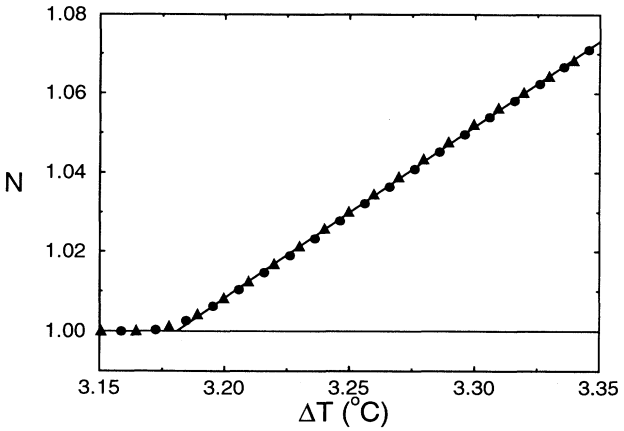

FIG. 4. The Nusselt-number results for $\Gamma=43$ which were used for the determination of ΔT_c. The data are for straight rolls (decreasing ΔT, ●) and for concentric rolls (increasing ΔT, ▲).

B. Amplitude and wave-number dependence on ϵ

The stabilization of concentric-roll patterns near onset without strong sidewall forcing permitted the investigation of the wave-number selection near onset and of the dependence of the amplitude on ϵ. The patterns were imaged with the shadowgraph visualization method. The relation between the measured intensity variation and the underlying temperature-field amplitude was studied previously by Rasenat *et al.* [35] for a conventional shadowgraph setup. For the shadowgraph configuration in our experiment, the results from the above paper could be applied with slight modifications.

In order to be certain that the shadowgraph images yielded reliable data, we measured the steady-state amplitude for straight-roll patterns for $0.001<\epsilon<0.10$. We let the parallel rolls relax to a steady state at $\epsilon=0.01$ for five horizontal thermal diffusion times before starting to take data by slowly changing ϵ in small steps. The rolls tended to end perpendicular to the sidewall; hence cross rolls formed at the two sides of the straight rolls as in Fig. 3(c). As ϵ increased, the cross-roll region grew, and the straight-roll wavelength decreased. When the cross rolls became too long, they shrank in size, inducing a sudden change in the number of straight rolls present. The ϵ value at which this event occurred varied from one run to the next but was typically between ϵ of 0.02 and 0.06. One image for each cell, composed by vertically stacking a $1d$ wide region across the center of the cell in increasing ϵ order, illustrates this pattern evolution in Fig. 5 ($\Gamma=41$) and Fig. 6 ($\Gamma=43$). As can be seen, the wave-number q for the straight rolls changed with ϵ. A plot of q measured along the line joining the two cross-roll patches for the $\Gamma=41$ cell is shown in Fig. 7 (solid squares). The wave number of the straight-roll pattern at onset is taken to be at the critical wave number $q_c=3.117$. For the straight-roll patterns, the compression by the cross rolls induced a wave-number distribution, and we show the standard deviation of q by the horizontal bars in the plot. The wave number jump at $\epsilon\approx0.04$ resulted from the

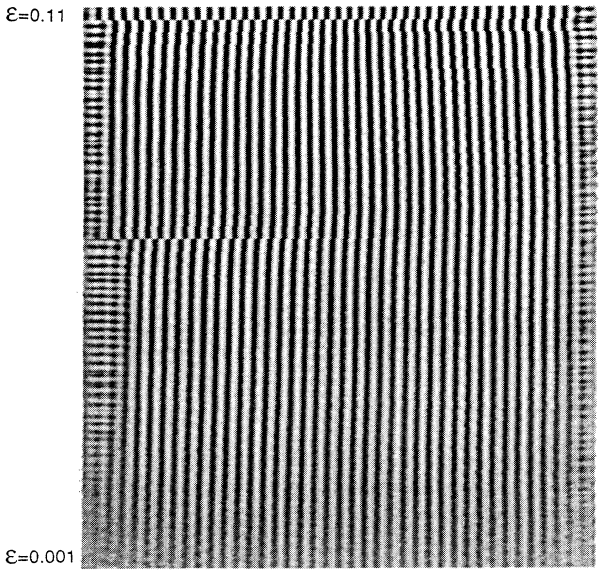

FIG. 5. Composite shadowgraph image showing straight-roll pattern evolution with ϵ for $\Gamma=41$.

change in cross-roll size as mentioned above. Also shown in the figure are the wave numbers of the concentric-roll pattern (solid circles) in the $\Gamma=41$ cell. Unlike that of the straight-roll patterns, the wave number of the concentric patterns did not vary measurably with the radial location. The wave number decreased very slightly with ϵ, and agreed to within experimental accuracy with the theoretical predictions by Manneville and Piquemal [24] and Buell and Catton [26].

For $\Gamma=43$, we made quantitative amplitude measurements of the straight rolls. To obtain the amplitude, we first divided a background image without convection by images taken with convection. This procedure yielded a linear relationship between the shadowgraph intensities and the convective amplitude as explained in Ref. [35]. A region of width $1d$ along the rolls and length $5d$ perpendicular to the rolls centered at the cell center was extracted and then averaged along its width to produce a

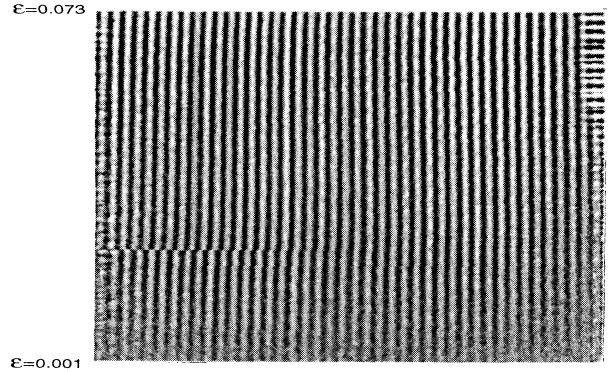

FIG. 6. Composite shadowgraph image showing straight-roll pattern evolution with ϵ for $\Gamma=43$.

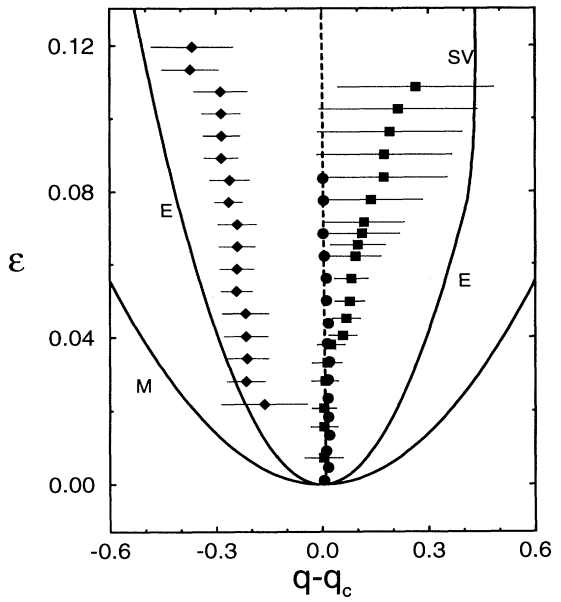

FIG. 7. ϵ dependence of wave numbers for $\Gamma=41$. Concentric rolls: ●. Straight rolls: ■. Cross rolls in the concentric patterns: ♦. Marginal stability curve: *M*. Ekhaus instability boundary: *E*. Skewed-varicose instability boundary: SV. The dashed line represents the theoretical prediction of the concentric-roll wave number. The wave number for straight rolls at onset was used to calibrate the length scale and was taken to be $q_c=3.117$.

one-dimensional data set consisting of 45 points $I(x)$. A fit of $I(x)=I_m+I_0\sin(qx+\phi)$ was performed. Here q is the wave number of the rolls and I_m is the mean intensity ratio. Ideally, I_m should be equal to 1, but the fits gave values over the range from 0.94 to 1.02. In general, I_0 would depend on the geometry of the shadowgraph setup, q, and ϵ; but we held the shadowgraph parameters constant and thus changes in I_0 were caused by changes in q and ϵ only. A plot a I_0^2 vs ΔT is shown in Fig. 8, and one can see the linear dependence for $\Delta T<3.42$ °C. Since there was some deviation of q from q_c, we fitted the data with the function $I_0=I_{00}[\epsilon-\xi_0^2(q-q_c)^2]^\beta$, which is based on the amplitude equation [12]. Here $\xi_0^2=0.148$, q is obtained from the fit to the data, and q_c is the average of q for $\epsilon<0.015$. It turned out that the q-dependent correction was essentially negligible. Since any nonuniformity of the cell can introduce variations of the local ΔT_c, we did not use the ΔT_c from the Nusselt-number measurement, which would be a global average. Instead we allowed ΔT_c to vary for all fits concerning amplitude variations. This produced $\Delta T_c=3.171\pm0.003$ °C, close to the Nusselt-number result, and $\beta=0.52\pm0.06$ in good agreement with the predicted exponent of 0.50.

Even in the more strongly forced cell $\Gamma=43$, the perturbation due to the sidewall forcing was quite small. It did not force rolls of detectable amplitude below $\epsilon=-0.006$. We can see this in Fig. 9, which is a plot of the shadowgraph intensities of the concentric rolls as a function of radius averaged over a 40° angular range. At $\epsilon=-0.008$ no convection was observable, but at

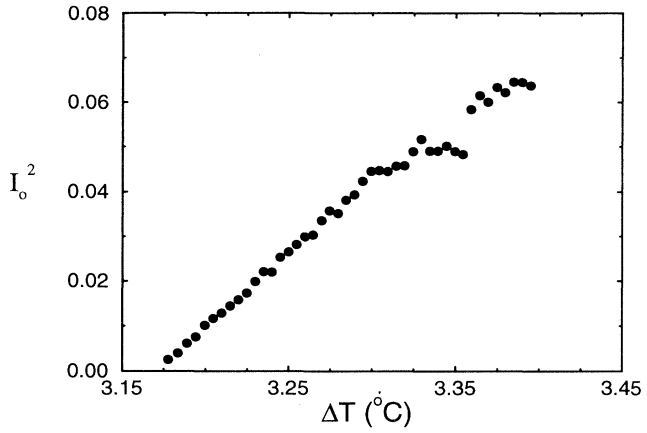

FIG. 8. I_0^2 vs ΔT for the center of the straight-roll pattern for $\Gamma=43$.

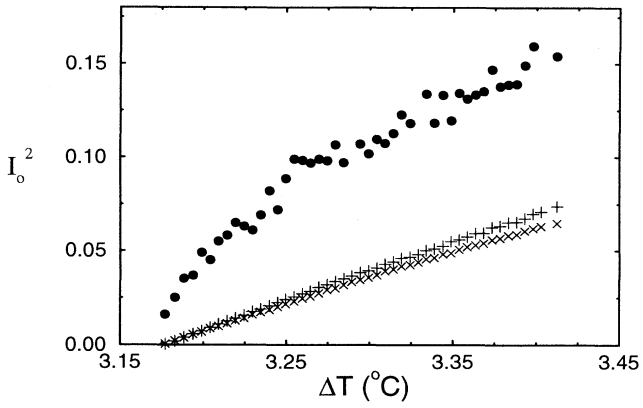

FIG. 10. I_0^2 vs ΔT for concentric-roll patterns and $\Gamma=43$. Umbilicus: ●. Envelope averaged from −10° to 10°: ×. Envelope averaged from 170° to 190°: +

$\epsilon=-0.004$, five roll pairs were detectable near the sidewall ($r=43$). The umbilicus ($r=0$) had a higher amplitude than the rolls situated at larger r, but the difference decreased with increasing ϵ. For $\epsilon=0.007$ the umbilicus amplitude is more than twice that of the envelope region (the region with an approximately constant amplitude outside the umbilicus) whereas for $\epsilon=0.035$ the ratio is only about 1.7. This indicates that the umbilicus grows more slowly with ϵ over this range of ϵ. Also noticeable is the influence of the finite correlation length near the sidewall, where the amplitude grows noticeably over a range varying from about $15d$ at $\epsilon=0.007$ to about $7d$ at $\epsilon=0.035$. To get the amplitude of the umbilicus for a concentric pattern, we took a $0.8d\times0.8d$ region around the umbilicus (9×9 pixels) and fitted the intensity to the function $I(x,y)=I_m+I_0+I_1[(x-x_0)^2+(y-y_0)^2]$. Since I_m is correlated with I_0, we set I_m equal to the mean of the entire image; of course, it once more was within a few percent of unity. The parameter I_0 is proportional to the amplitude at the umbilicus which is located at (x_0,y_0). For the envelope, we averaged the intensity azimuthally over a 20° angular range to get $I(r)$ and fitted $I(r)$ to $I(r)=I_m+I_0\sin(qr+\phi)$ over the range $10d<r<22d$. The results for the umbilicus, and for the envelope at two directions 180° apart, are plotted in Figs. 10 and 11. The difference in the ϵ dependence of the amplitude at the umbilicus and away from it is apparent in these figures. The slight difference obtained for the envelope in the two opposite directions is the result of shadowgraph contrast variations caused by optical imperfection. As can be seen by comparison with Fig. 8, the amplitude of the envelope region is very close to that of the straight-roll pattern at the same ϵ. This is expected from the Nusselt-number measurement, which showed that the heat transports were very close for the two different patterns. The contribution of the umbilicus to the heat transport is small despite its higher amplitude since it accounts for only a very small portion of the total area. Because the wavelength did not change with radius, we fitted the data, again allowing ΔT_c to vary, with $I_0=I_{00}\epsilon^{\beta_2}$ for $0.01\le\epsilon\le0.06$ and obtained $\beta_2=0.48\pm0.04$ for the region outside the umbilicus.

The growth of the umbilicus with ϵ depends on the

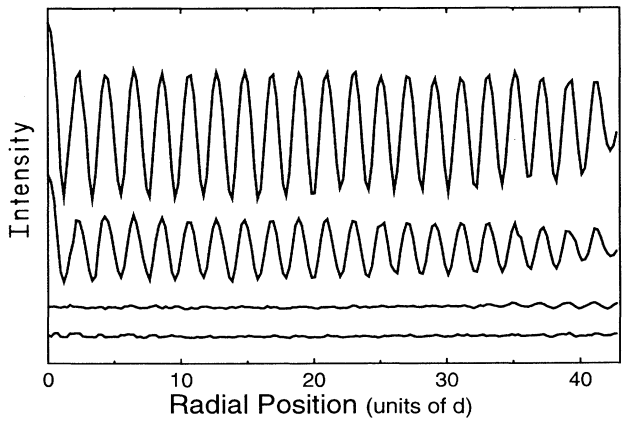

FIG. 9. Shadowgraph intensity vs radial position for concentric rolls and $\Gamma=43$. Top to bottom: $\epsilon=0.035$, 0.007, −0.004, and −0.008.

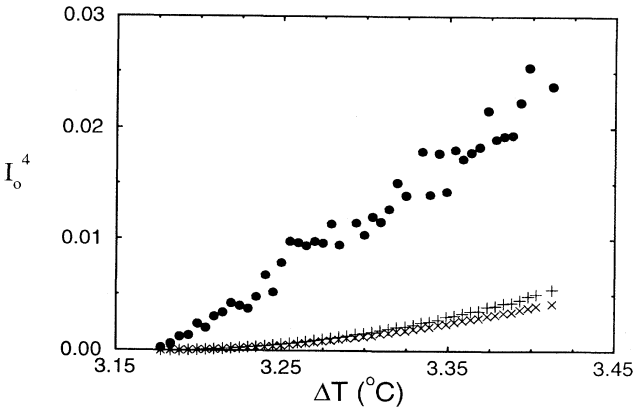

FIG. 11. I_0^4 vs ΔT For concentric-roll patterns and $\Gamma=43$. Umbilicus: ●. Envelope averaged from −10° to 10°: ×. Envelope average from 170° to 190°: +.

competition between finite size effects and the increase of ϵ. For sufficiently small ϵ it grows like $\epsilon^{1/2}$; but when $\epsilon \approx (\Gamma\pi)^{-1}$ ($=0.008$), it is expected to grow as $\epsilon^{1/4}$ [11]. In their simulation for $\Gamma=32$, Pomeau, Zaleski, and Manneville [11] found this $\epsilon^{1/4}$ behavior to extend up to $\epsilon=0.04$, beyond which higher-order nonlinearities caused the effective exponent to be larger than $\frac{1}{4}$. Our shadowgraph resolution and cell uniformity were not suitable for investigations of the $\epsilon^{1/2}$ scaling at very small ϵ but did allow us to explore the $\epsilon^{1/4}$ scaling of the umbilicus. Our result for the umbilicus, $I_0 = I_{00}\epsilon^{0.27\pm0.004}$ for $0.005 \le \epsilon \le 0.060$, confirms the theoretical predictions.

IV. SECONDARY INSTABILITIES

A. Instability of the axisymmetric pattern

The first instability encountered by concentric-roll patterns as ϵ is increased has been well established [4,6,16]. The generic feature from these experiments in fluids covering the low- to high-Prandtl-number range is an off-center shift of the umbilicus. This change in the umbilicus position is now understood to be caused by the focus instability that arises from the competition between roll phase diffusion and a large-scale flow field [28,29]. The threshold for this instability is expected to depend on both the Prandtl number of the fluid and the aspect ratio of the cell [29]. The two different sidewalls in our experiments had considerably different forcing strengths, and we found that the one with the greater forcing enhanced the stability of the concentric pattern.

In the Introduction we discussed the evolution of the pattern beyond the focus instability. For low Prandtl numbers and modest aspect ratios it involved local wave-number distortion and nucleation of dislocations, a process apparently related to the skewed-varicose instability. An interesting question then arises about what would happen if the skewed-varicose instability did not occur. This can be studied in a larger-aspect-ratio cell. For a given umbilicus displacement the compression-induced wave-number change is proportional to $1/\Gamma$, and thus for large enough aspect-ratio cells, the skewed-varicose instability boundary would not be crossed even for a significant umbilicus displacement. Indeed, in our larger cells, we find new instability mechanisms involving the emission of traveling waves by the umbilicus, as well as transients during which the umbilicus moves from the cell center all the way to the wall. Below we concentrate first on the less-forcing wall with the spoiler tab ($\Gamma=41$).

In the $\Gamma=41$ cell, the umbilicus started at the geometric center of the cell at onset, and as ϵ increased, it moved very slightly off center. Meanwhile, the pattern remained stable and time independent. The amount of static off center shift depended weakly on the ϵ ramp speed, but even a quasistatic ramp caused a measurable shift in the umbilicus position. The shift was always less than $\frac{1}{2}d$ (1.2% of the cell radius) for time-independent patterns. With that in mind, we adopted a relatively fast ramp, going from $\epsilon=-0.02$ to 0.093 in 16 equally spaced steps while waiting $400\tau_v$ at each step. The umbilicus positions at the various ϵ steps are shown in Fig. 12 as solid circles. At $\epsilon=0.093$, the system was allowed to equilibrate for $1200\tau_v$. During that time the umbilicus had moved about $\frac{1}{2}d$ away from its initial position, to the point shown by the up-pointing solid triangle in Fig. 12. The pattern at that point became time dependent. A radially traveling wave appeared. It was caused by the repeated sudden emission of a new concentric roll by the umbilicus, followed by a much longer quiet period. The umbilicus moved abruptly with the emission of each new roll. As the wave propagated outward, the umbilicus relaxed slowly to a new position. The umbilicus position is given by the solid line in Fig. 12. A detailed view of approximately one cycle of the umbilicus emitting the wave is shown in Fig. 13. To see the traveling wave more clearly, we took 30° wedges centered at the umbilicus for two opposite directions, and averaged the intensity azimuthally for each wedge. The result was then processed into a space-time plot, with a typical one shown in Fig. 14. It is apparent from Fig. 13 as well as from Fig. 14 that the fluid flow at the umbilicus did not vary sinusoidally, but rather varied in a step-function-like manner. The time between each emission of a new roll was not constant, but it is clear from the figure that the interval is quite long, on the order of one to two horizontal diffusion times. For $0.08 < \epsilon < 0.10$, the umbilicus typically emitted a new roll from 3 to 12 times and then stopped when it had returned to within $\frac{1}{3}d$ of the geometric center of the cell. For the particular run described above, this is shown by the down-pointing triangle in Fig. 12. The pattern was time independent afterwards.

Traveling waves in axisymmetric patterns had been predicted by Tuckerman and Barkley [36] for cells with conducting sidewalls. These waves seem to be unrelated to our experimental observation. They were periodic, traveled from the wall to the center, and were nearly sinusoidal in shape. As discussed above, in the experimental system the waves traveled in the opposite direc-

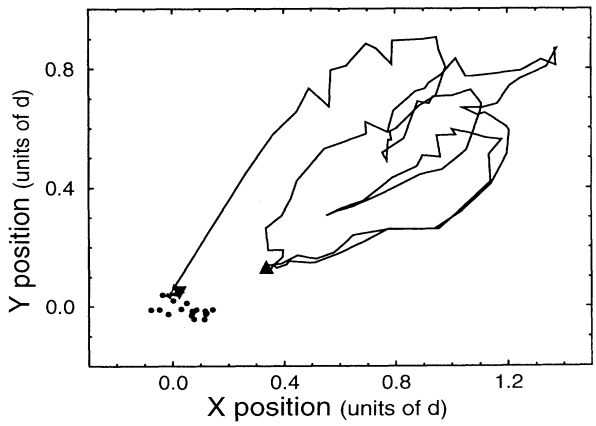

FIG. 12. Positions of the umbilicus for $\Gamma=41$. ● are for the ϵ steps at the beginning of the run up to $\epsilon=0.093$. ▲ is the position after equilibration at $\epsilon=0.093$ when the roll emission by the umbilicus started. ▼ is the final position when the roll emission stopped. The solid line shows the umbilicus positions during the run.

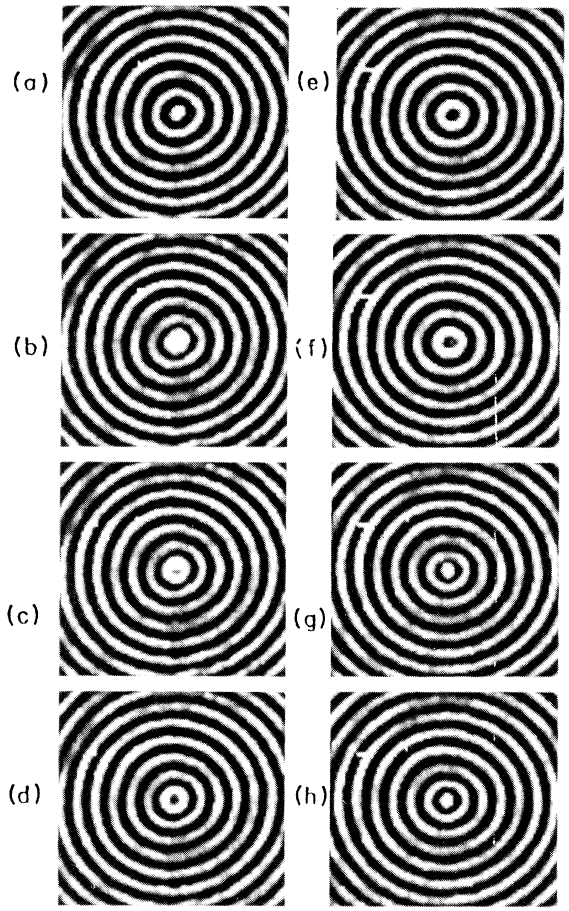

FIG. 13. Magnified view of the umbilicus emitting a radially traveling wave at $\epsilon=0.099$ and for $\Gamma=41$. Elapsed times (arb. orig.) are (a) 0, (b) $100\tau_v$, (c) $200\tau_v$, (d) $300\tau_v$, (e) $1300\tau_v$, (f) $1400\tau_v$, (g) $1500\tau_v$, (h) $1600\tau_v$.

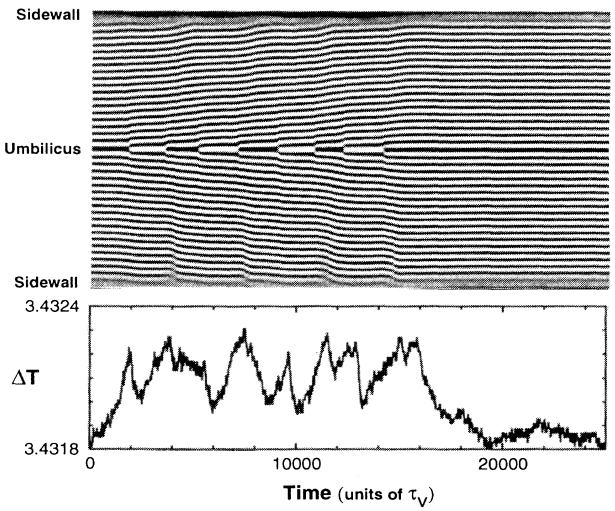

FIG. 14. Space-time plot of radially traveling wave at $\epsilon=0.098$, and corresponding ΔT variations (in °C) for $\Gamma=41$.

tion, were highly asymmetric, and were nonperiodic.

The time dependence of the pattern is correlated with the global heat transport, as seen in Fig. 14. Between the emission of new rolls, while the pattern was steady, the heat transport was large and thus ΔT decreased. During the emissions ΔT was high, corresponding to reduced heat transport. The variation in ΔT was exceedingly small, only around 0.4 mK, which corresponded to a 0.03% change in the heat transport.

For $\epsilon \geq 0.10$, the umbilicus initially moved in a manner similar to that shown by the solid line in Fig. 12. However, it never returned to the cell center. Instead, it continued emitting and eventually moved far away from the cell center toward the sidewall. This sequence of events is illustrated in Fig. 15. The umbilicus speed during this process is shown in Fig. 16. It initially increased linearly with the distance from the center until the umbilicus had traveled about half the distance to the sidewall, and then increased even more rapidly. In the end, the umbilicus collided with the sidewall and disappeared, and a time-dependent straight-roll pattern with several defects remained.

Coupled to the radially traveling waves was the movement of the cross rolls near the sidewall. Below $\epsilon=0.08$, where the concentric pattern was time independent, the cross rolls also were time independent. As ϵ was in-

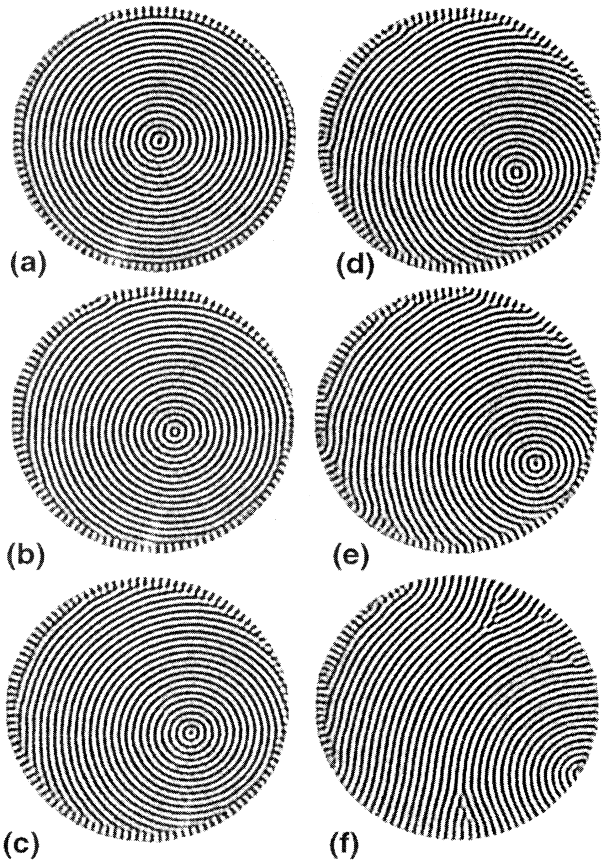

FIG. 15. Destruction of concentric-roll pattern at $\epsilon=0.102$ and for $\Gamma=41$. Elapsed times (arb. orig.) are (a) 0, (b) $5600\tau_v$, (c) $7800\tau_v$, (d) $8520\tau_v$, (e) $9240\tau_v$, (f) $9840\tau_v$.

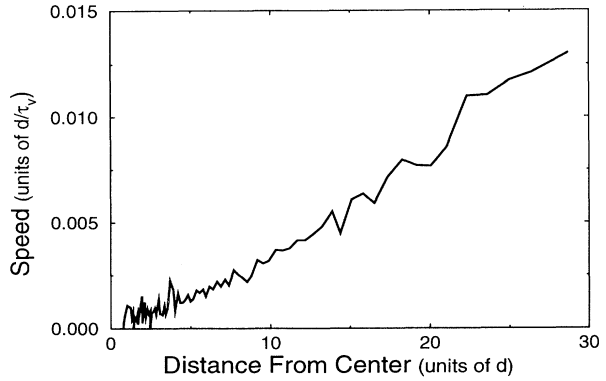

FIG. 16. The radial umbilicus speed as a function of its radial position. The data are for $\Gamma=41$ and $\epsilon=0.102$.

creased from 0 to 0.08, however, three cross-roll pairs were lost and the cross-roll wave number changed. This is shown by the diamonds in Fig. 7. There the steps in q correspond to the roll-pair losses. The horizontal bars indicate the standard deviation of q due to its azimuthal variation. We see that the cross-roll wave number was close to the left Eckhaus instability boundary, and as ϵ increased, the wave number decreased. For $\epsilon>0.08$, where the umbilicus was displaced from the center and emitted the traveling wave, the cross rolls traveled azimuthally, and a cross-roll source and sink were present. The source was situated in the direction of the umbilicus displacement from the center, while the sink was approximately opposite it. Figure 17(a) shows a space-time plot

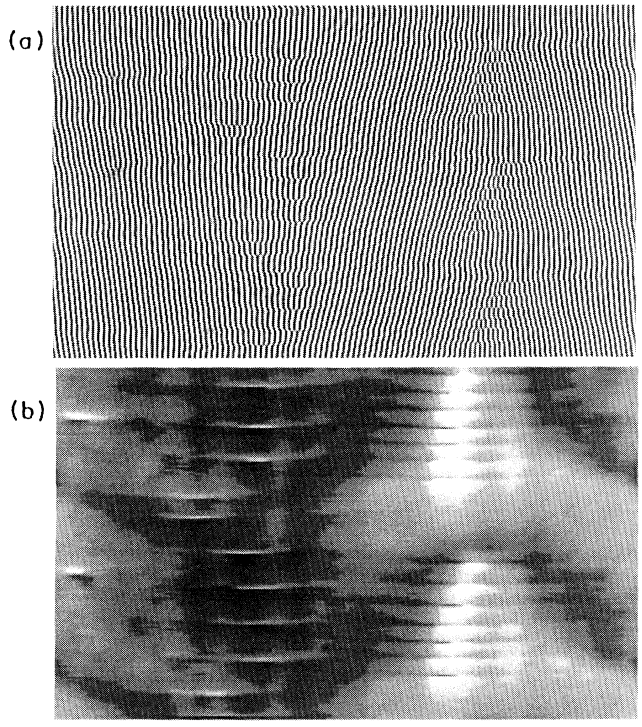

FIG. 17. Space-time plot of cross rolls for $\epsilon=0.099$ and $\Gamma=41$. Time increases in the upward direction, and the images cover $6930\tau_v$. The horizontal axis covers 360°. (a) Shadowgraph intensity of the rolls. (b) Grey-scale-coded wave numbers of the rolls (white: large wave numbers).

of the cross-roll dynamics. The source and sink regions are enlarged in Figs. 18 and 19. There was an obvious asymmetry between roll creations at the source and annihilations at the sink. New roll pairs were created at relatively uniform time intervals, but roll destructions usually occurred in batches of 6–8 roll pairs.

The traveling nature of the cross rolls, and existence and positions of the source-sink pair, suggest that a large-scale flow was present in the cell when the umbilicus was off center. It is known that in low-Prandtl-number convection, the roll curvature induces a large-scale flow which in turn interacts with the rolls [27]. In a strictly axisymmetric pattern, no net large-scale flow is expected in any direction. This is not true, however, when the umbilicus is away from the center of the cell. In an experiment by Croquette *et al.* [28], large-scale flow was shown to move from the umbilicus toward the nearest sidewall, with backflow along the sidewall. If the same situation existed in our experiment, then the large-scale flow would travel from the source to the sink along the wall, i.e., in the same direction as the motion of our cross rolls.

Using a sliding window of width 10 rolls to perform Fourier transforms on the cross rolls, we obtained their local wave numbers. A typical result for $\epsilon=0.09$ during the time-dependent phase is shown in Fig. 20. The spatiotemporal behavior of the wave numbers is shown in Fig. 17(b). The sink region had a larger and the source a smaller wave number. This is similar to results obtained in an annulus [28], where rolls in the presence of through flow were shown to develop a wave-number gradient. The through flow was imposed by running fluid from an inlet to an outlet, with the outlet located opposite the inlet. The rolls near the inlet had smaller wave numbers while near the outlet they had larger ones. On the basis of the existence of the source-sink pair, the traveling nature of the cross rolls, and the wave-number gradient, we believe that the behavior of the cross rolls was strongly influenced by a large-scale flow which existed for the off-center concentric-roll patterns.

The interaction between the cross rolls and the concentric rolls was complex. At small ϵ, where the umbilicus

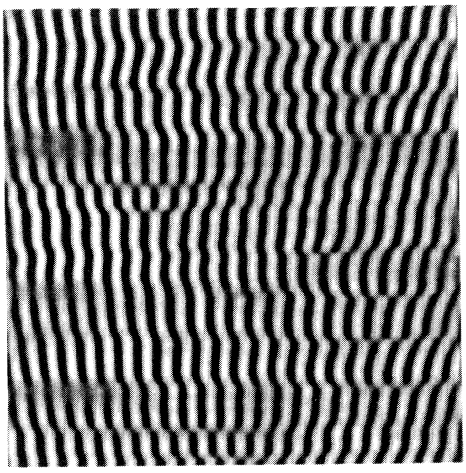

FIG. 18. Enlargement of the source region of Fig. 17(a).

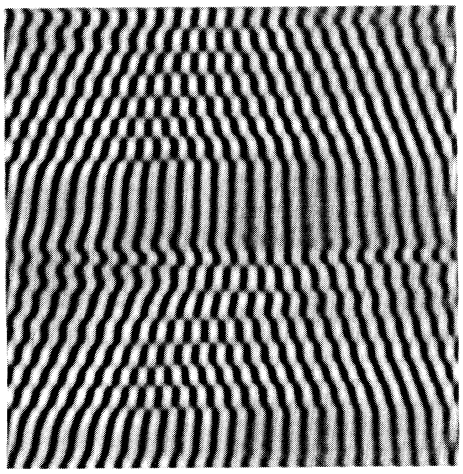

FIG. 19. Enlargement of the sink region of Fig. 17(a).

was not emitting, the cross rolls were stationary, except for some wave-number adjustment when ϵ was changed. The cross-roll wavelength increased with ϵ. This was achieved through destruction of rolls near the sink region. At larger ϵ, where the umbilicus was off center, complicated cross-roll dynamics existed. As soon as the source first started to create new rolls, the umbilicus started emitting. While the source activities preceded the umbilicus activities in most runs, there were several occasions when the reverse was true. The sink usually was the last location (among the source, sink and umbilicus) for activity to start, but the source would sometimes create new rolls long after the sink had stopped roll destructions. The complexity of the cross-roll and concentric-roll interactions arose from wave-number-distortion fields that were hard to quantify. Our interpretation of the observed events is that the large-scale flow generated by the emitting umbilicus drove the cross-roll motions through wave-number distortion. The sequence consisting of the umbilicus emitting and cross-roll creation or annihilation was determined by residual wave-number stress, which could vary with the past history of the events. Thus each time sequence was slightly different, the details depending on the wave-number distortion that persisted following an emission at the umbilicus.

The more forcing sidewall without a spoiler tab stabilized the concentric patterns to higher ϵ. The sequence of events, illustrated in Fig. 21, was in part similar to that for the sidewall with a spoiler tab. The umbilicus would shift as ϵ increased, and at $\epsilon \approx 0.19$, the roll next to the wall along the direction of the umbilicus would pinch off, resulting in a pair of defects next to the wall. The defects moved apart along the sidewall, and two small patches of cross rolls formed and traveled with the defects. Before the defects had reached the opposite end of the sidewall from their origin, a new defect pair formed while the umbilicus would emit a new circular roll. Each emission was accompanied by a pair of defects, but a defect pair always appeared before the umbilicus started emitting. The umbilicus would travel toward the sidewall, and its annihilation left a time-dependent pattern of mostly straight rolls. There was no window in ϵ in which the umbilicus would return to the cell center following a roll emission, so the radially traveling wave always led to destruction of the concentric patterns.

The radially traveling waves were the major charac-

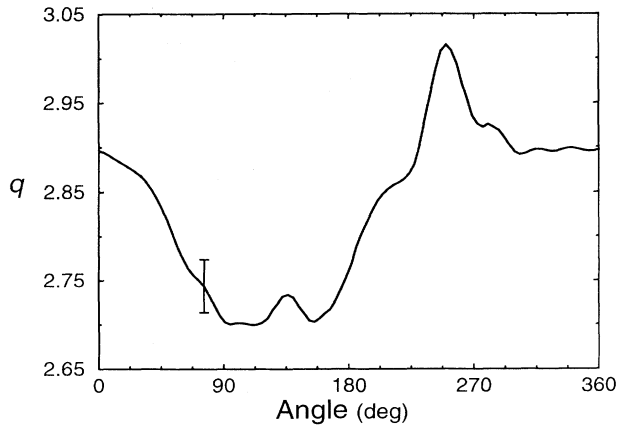

FIG. 20. Cross-roll wave number as a function of angular position for $\epsilon = 0.090$ and $\Gamma = 41$ during the traveling-wave phase.

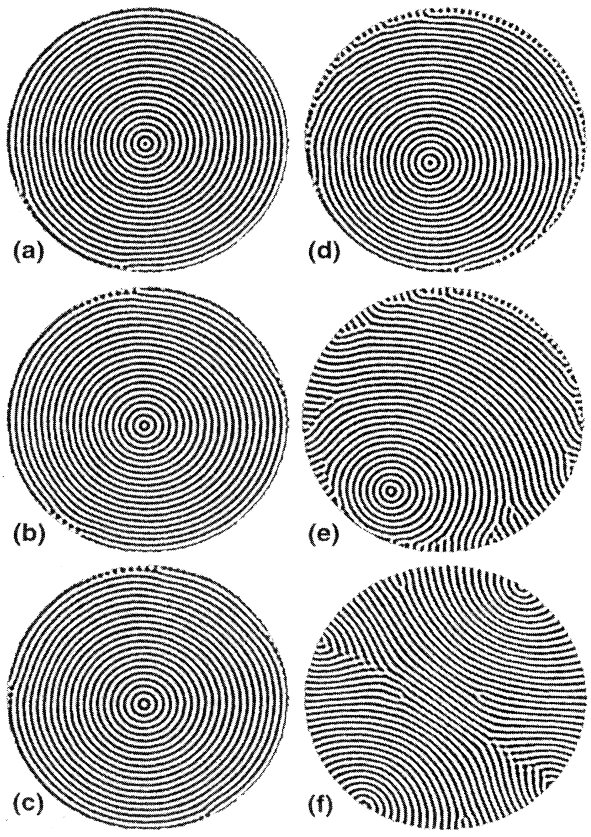

FIG. 21. Destruction of concentric-roll pattern at $\epsilon = 0.20$ and for $\Gamma = 43$. Elapsed times (arb. orig.) are (a) 0, (b) $1500\tau_v$, (c) $4000\tau_v$, (d) $7600\tau_v$, (e) $9600\tau_v$, (f) $10\,600\tau_v$.

teristic of the evolution of patterns beyond the focus instability. The signature of the skewed-varicose instability of roll pinching and defect propagation could be avoided, indicating that in these larger-aspect-ratio cells wave-number distortion was sufficiently reduced. One can compare our experimental results with theoretical predictions for the focus instability [29] which indicated that the axisymmetric patterns would become unstable at $\epsilon=0.18$ for our Prandtl number of 0.93 [37]. Since the calculation assumed rigid sidewalls, the appropriate comparison is with the straight sidewall experiment (as opposed to the wall with a spoiler tab). Our experimental value of $\epsilon=0.16\pm0.02$ is quite close to the calculated values. However, theoretical studies have not yet been extended to a stability analysis of the state which forms beyond the focus instability. In past experiments on smaller systems the stable state had been found to be a static umbilicus shift where large-scale flows are balanced by wave-number distortions. In our work with the larger aspect ratios the axisymmetric state destabilized completely and the umbilicus traveled out to and collided with the sidewall. It is apparent that both the sidewall forcing and the aspect ratio of the system need to be considered in the theoretical analysis.

B. Instability of straight-roll pattern

Straight-roll patterns in a low-Prandtl-number fluid confined in a cylindrical container have been studied extensively by Croquette [4,14] for cells with $\Gamma=7.66$ and 20. In a small-Γ cylindrical cell, there were two focus singularities bracketing the region of parallel straight rolls. The rolls tended to bend toward the singularities as ϵ was increased, resulting in compression of rolls along the line connecting the singularities. When the compression became too large, the rolls in the center of the cell, where the compression was most severe, underwent a skewed-varicose-like instability. For $\Gamma=7.66$, this first occurred at $\epsilon=0.13$. One compressed-roll pair got pinched off, nucleating two defects. These two defects climbed along the roll axis to within one or two wavelengths of the sidewall and then glided along the wall to disappear into the focus singularities. When the defects disappeared, the singularities nucleated a new roll pair, resulting in a pattern containing the same number of rolls as before. This process then repeated itself. In the large-Γ case, the process was similar, except the onset of time dependence was at the lower $\epsilon=0.085$. In addition, instead of two focus singularities, two domains of short cross rolls existed on the two sides of the straight rolls. The onset of this instability has been demonstrated to be the result of a large-scale flow [38]. If the flow is suppressed, the tendency for the rolls to end more perpendicular to the sidewall at higher ϵ is also suppressed, and the straight-roll state was observed to be stable to ϵ as large as about 0.6.

Our observation of the straight-roll instability was carried out primarily in the $\Gamma=41$ cell with the spoiler tab because the spoiler tab was expected to reduce the strength of the large-scale flow in the region of convection [38]. However, the instability occurred at about the same ϵ value for the two cells. The pattern evolution was similar to previous observations, but the details were somewhat different. The straight-roll patterns were produced in the same manner as in the investigation of the amplitude dependence on ϵ. The patterns were time dependent for $\epsilon>0.095$, close to the value observed by Croquette for a cell of half the aspect ratio. The wave-number distribution of the rolls, obtained from the distribution in the magnitude of local wave vectors, is indicated by the squares and horizontal bars plotted in Fig. 7. One sees that time dependence set in when some local wave number (the wave number near the cell center) crossed the skewed-varicose instability boundary. Defects were created at the central region of the cell and moved to the sidewall. There were always defects that stayed near the sidewall while the central region of the cell underwent the skewed-varicose-like instability, even when time dependence first set in. New defects were created not by the pinching of just a single roll, but by a

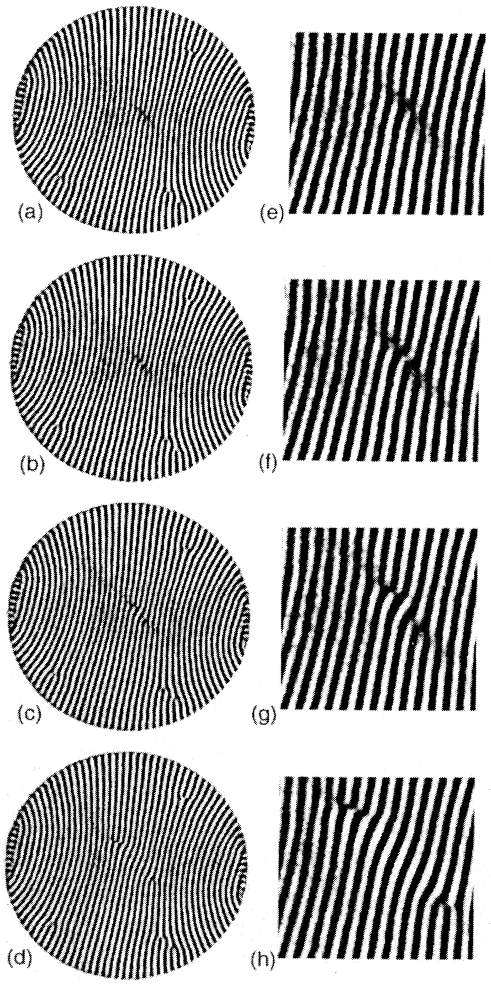

FIG. 22. Defect nucleation mechanism for straight rolls at $\epsilon=0.115$ and for $\Gamma=41$. On the left the entire cell is shown. The right gives a magnified central portion. Elapsed times (arb. orig.) are (a) 0.0, (b) $1.3\tau_v$, (c) $2.6\tau_v$, (d) $9.0\tau_v$, (e) $0.0\tau_v$, (f) $1.3\tau_v$, (g) $2.6\tau_v$, and (h) $9.0\tau_v$.

pinching and reconnection of two adjacent rolls. The two defects then executed both climbing and gliding motion and moved toward the sidewall in an oblique manner. They then joined with the defects already present near the sidewall, and a long-time reorganization of the defects began as some defects merged into the focus singularities or cross rolls. The whole sequence of events, including magnified central regions, is illustrated in Fig. 22. The time scale for the nucleation and the initial movement to the sidewall was still quite fast, taking only a few τ_v. The frequency of the nucleation increased with increasing ϵ up to $\epsilon \sim 0.12$. Beyond that the system became much more disorganized spatially with defects and grain boundaries evolving in an irregular fashion.

C. Pattern evolution at larger ϵ

Finally, we mention briefly what happens as ϵ is increased well beyond the first instability point of either the straight or the concentric rolls. The sequence of events which occurs with quasistatically increasing ϵ is illustrated in Fig. 23. As was reported by Morris, Bodenschatz, Cannell, and Ahlers (MBCA) [31] for $\sigma = 0.96$ and a cell with $\Gamma = 78$, the pattern first develops three or four focus singularities along the sidewall and considerable roll curvature throughout. For ϵ greater than about 0.6, small spirals begin to form in the cell interior. With increasing ϵ, the spirals become more abundant until the state described by MBCA as "spiral defect chaos" [31] is reached. Our cell is not large enough to make a quantitative comparison of the statistical properties of this state with those measured by MBCA, but qualitatively the two experiments reveal the same phenomenon. This is noteworthy since our sample, by virtue of being twice as thick and having a much smaller ΔT_c, comes significantly closer to satisfying the Boussinesq approximation. The parameter $\mathcal{P}_c$ defined by MBCA (Ref. 11 of Ref. [31]) and by Busse [39] is -0.31 in our case, i.e., its magnitude is a factor of 2.3 smaller than the smallest value explored by MBCA. We believe that this removes any doubt about spiral-defect chaos being a natural state of the large Boussinesq system with σ near one.

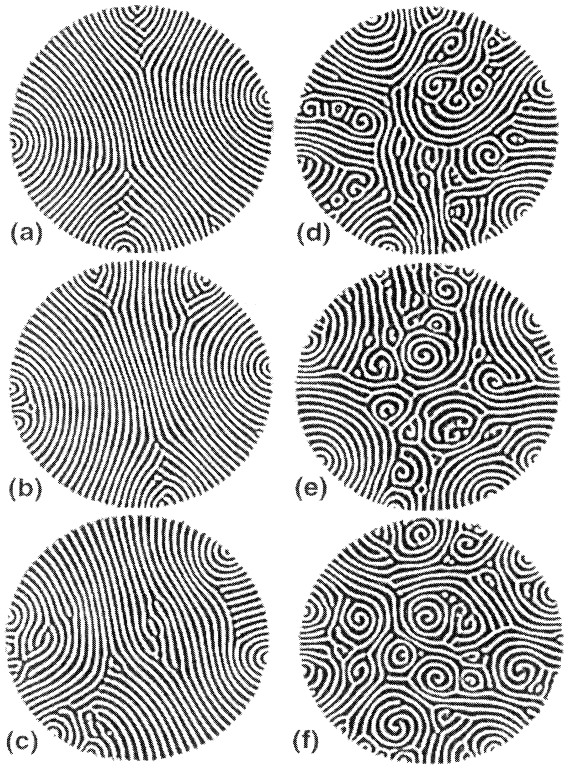

FIG. 23. Typical patterns for $\Gamma = 41$ and $\epsilon =$ (a) 0.34, (b) 0.47, (c) 0.61, (d) 0.75, (e) 0.88, and (f) 0.89.

V. CONCLUSION

Axisymmetric patterns were stabilized with adjustable static sidewall forcing in a low-Prandtl-number fluid, CO_2. The forcing was weak enough that the amplitude near onset was not affected, and we were able to measure how the amplitude changed with ϵ for axisymmetric patterns. The amplitude at the umbilicus was proportional to $\epsilon^{0.27\pm0.04}$ in agreement with the theoretical predictions of Pomeau, Zaleski, and Manneville [11] while outside the umbilicus it varied as $\epsilon^{0.48\pm0.04}$, consistent with an amplitude-equation description of the pattern [12].

A weakly forcing sidewall was constructed by adding a spoiler tab [32,33] to the sidewall midplane. Concentric rolls were the preferred patterns at onset in this system. The coexistence of cross rolls confined to a narrow band near the sidewall and the concentric rolls was the major new feature. These patterns were stable and time independent up to $\epsilon = 0.08$. At higher ϵ, a radially traveling wave was emitted by the off-center umbilicus as a consequence of the focus instability for axisymmetric patterns. For ϵ between 0.08 and 0.10, the traveling wave existed while the umbilicus was off center, but the pattern became time independent after the umbilicus found its way back to the cell center. Even though the traveling-wave state was a transient, it could last for a very long time, up to 25 horizontal thermal diffusion times in some cases. Since the movement of the umbilicus appeared random and did not follow any definite pattern, it may be that the traveling-wave state could persist indefinitely; but in all of our runs the umbilicus found the center of the cell after some time and the time dependence ceased. Above $\epsilon = 0.10$, the umbilicus never returned to the center, and instead the pattern lost its stability to straight-roll patterns via the movement of the umbilicus toward the wall. That motion was accompanied by the emission of the radially traveling waves. Sidewall forcing was seen to stabilize the onset of the focus instability, as a more strongly forcing sidewall inhibited the radial waves up to $\epsilon \approx 0.19$. For this sidewall, the radially traveling wave always resulted in the destruction of the concentric patterns.

The existence of the cross rolls next to the sidewall offered a probe for the large-scale flows that are especially important in pattern dynamics in low-Prandtl-number convection. We have shown that cross-roll creation and annihilation could be traced to the effect of a large-scale flow present in a nonaxisymmetric concentric-roll pattern. However, the relationship between these cross rolls and the concentric rolls is poorly understood. Owing to

the low-Prandtl-number fluid used in this experiment, we expect that the interplay between the large-scale flows and the small-scale roll flows is extremely complicated. The situation might be more tractable for experiments done in moderate-Prandtl-number fluids, although the existence of the traveling-wave state may depend critically on strengths of the large-scale flows and therefore may not be present at higher Prandtl numbers.

ACKNOWLEDGMENTS

We gratefully acknowledge support from a UC/LANL INCOR grant and from the U.S. Department of Energy. We also thank Ning Li for many useful discussions, Mike Cross for helpful remarks, and Alan Newell and Thierry Passot for providing data of the focus instability from their calculations.

[1] S. Chandrasekhar, *Hydrodynamic and Hydromagnetic Stability* (Oxford University Press, Oxford, 1961).

[2] H. Bénard, Rev. Gen. Sci. Pure Appl. **11**, 1261 (1900); **11**, 1309 (1900); Ann. Chem. Phys. **23**, 62 (1901); Lord Rayleigh, Philos. Mag. **32**, 529 (1916). Since this early work, a large literature pertaining to this field has evolved. Particularly useful as a guide are the reviews by E. L. Koschmieder [Adv. Chem. Phys. **26**, 177 (1974); in *Order and Fluctuations in Equilibrium and Nonequilibrium Statistical Mechanics,* edited by G. Nicolis, G. Dewel, and J. W. Turner (Wiley, New York, 1981), p. 169]; by F. Busse [in *Hydrodynamic Instabilities and the Transition to Turbulence,* edited by H. L. Swinney and J. P. Gollub (Springer, Berlin, 1981), p. 97; Rep. Prog. Phys. **41**, 1929 (1978)]; and by R. P. Behringer [Rev. Mod. Phys. **57**, 657 (1985)].

[3] M. Cross and P. Hohenberg, Rev. Mod. Phys. **65**, 851 (1993).

[4] V. Croquette, Contemp. Phys. **30**, 153 (1989).

[5] E. Koschmieder and S. Pallas, J. Heat Mass Transfer **17**, 991 (1974).

[6] V. Steinberg, G. Ahlers, and D. Cannell, Phys. Scr. **32**, 534 (1985).

[7] S. Ciliberto, E. Pampaloni, and C. Pérez-García, Phys. Rev. Lett. **61**, 1198 (1988).

[8] E. Bodenschatz, J. de Bruyn, G. Ahlers, and D. Cannell, Phys. Rev. Lett. **67**, 3078 (1991).

[9] M. Heutmaker and J. Gollub, Phys. Rev. A **35**, 242 (1987).

[10] M. Cross, Phys. Rev. A **25**, 1065 (1982).

[11] Y. Pomeau, S. Zaleski, and P. Manneville, Z. Angew. Math. Phys. **36**, 368 (1985).

[12] G. Ahlers, M. C. Cross, P. C. Hohenberg, and S. Safran, J. Fluid Mech. **110**, 297 (1981).

[13] M. Cross, P. Hohenberg, and M. Lücke, J. Fluid Mech. **136**, 169 (1983).

[14] V. Croquette, Contemp. Phys. **30**, 113 (1989).

[15] V. Croquette, M. Mory, and F. Schosseler, J. Phys. (Paris) **43**, 293 (1983).

[16] V. Croquette and A. Pocheau, in *Cellular Structures in Instabilities,* edited by J. Wesfreid and S. Zaleski, Lecture Notes in Physics Vol. 210 (Springer-Verlag, New York, 1984), p. 106.

[17] A. Newell and J. Whitehead, J. Fluid Mech. **38**, 279 (1969).

[18] L. Segel, J. Fluid Mech. **38**, 203 (1969).

[19] P. Bergé, M. Dubois, P. Manneville, and Y. Pomeau, J. Phys. (Paris) Lett. **41**, L431 (1980).

[20] M. Dubois and P. Bergé, J. Fluid Mech. **85**, 641 (1978).

[21] S. N. Brown and K. Stewartson, Proc. R. Soc. London Ser. A **360**, 455 (1978).

[22] V. Croquette, P. Le Gal, and A. Pocheau, Phys. Scr. **T13**, 135 (1986).

[23] M. Cross, Phys. Rev. A **27**, 490 (1983).

[24] P. Manneville and J. Piquemal, Phys. Rev. A **28**, 1774 (1983).

[25] J. Buell and I. Catton, J. Fluid Mech. **171**, 477 (1986).

[26] J. Buell and I. Catton, Phys. Fluids **29**, 23 (1986).

[27] E. Siggia and A. Zippelius, Phys. Rev. Lett. **47**, 835 (1981).

[28] V. Croquette, P. Le Gal, A. Pocheau, and R. Guglielmetti, Europhys. Lett. **1**, 393 (1986).

[29] A. Newell, T. Passot, and M. Souli, J. Fluid Mech. **220**, 187 (1990).

[30] A. Pocheau, V. Croquette, and P. Le Gal, Phys. Rev. Lett. **55**, 1094 (1985).

[31] S. Morris, E. Bodenschatz, D. Cannell, and G. Ahlers, Phys. Rev. Lett. **71**, 2026 (1993).

[32] C. W. Meyer, G. Ahlers, and D. Cannell, Phys. Rev. Lett. **59**, 1577 (1987).

[33] C. Meyer, G. Ahlers, and D. Cannell, Phys. Rev. A **44**, 2514 (1991).

[34] G. Küppers and D. Lortz, J. Fluid Mech. **35**, 609 (1969).

[35] S. Rasenat, G. Hartung, B. I. Winkler, and I. Rehberg, Exp. Fluids **7**, 412 (1989).

[36] L. S. Tuckerman and D. Barkley, Phys. Rev. Lett. **61**, 408 (1988).

[37] A. C. Newell and T. Passot (private communication).

[38] F. Daviaud and A. Pocheau, Europhys. Lett. **9**, 7 (1989).

[39] F. Busse, J. Fluid Mech. **30**, 625 (1978).

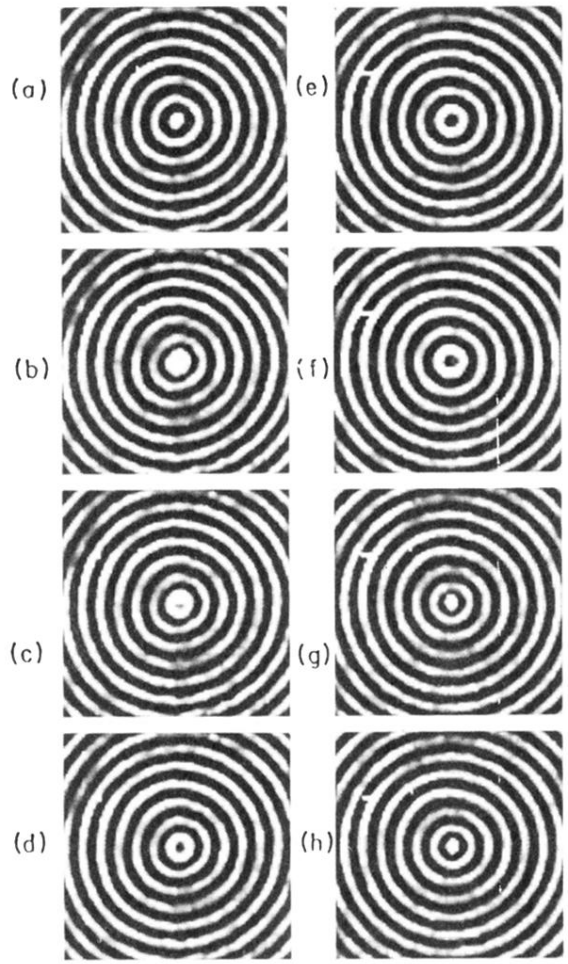

FIG. 13. Magnified view of the umbilicus emitting a radially traveling wave at $\epsilon=0.099$ and for $\Gamma=41$. Elapsed times (arb. orig.) are (a) 0, (b) $100\tau_v$, (c) $200\tau_v$, (d) $300\tau_v$, (e) $1300\tau_v$, (f) $1400\tau_v$, (g) $1500\tau_v$, (h) $1600\tau_v$.

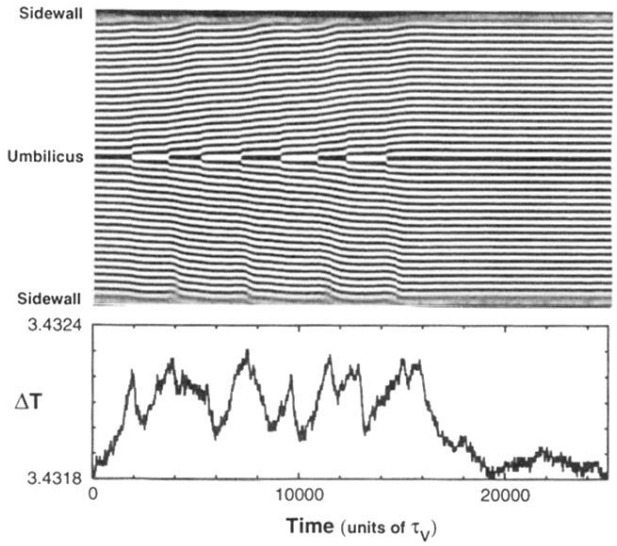

FIG. 14. Space-time plot of radially traveling wave at $\epsilon = 0.098$, and corresponding ΔT variations (in °C) for $\Gamma = 41$.

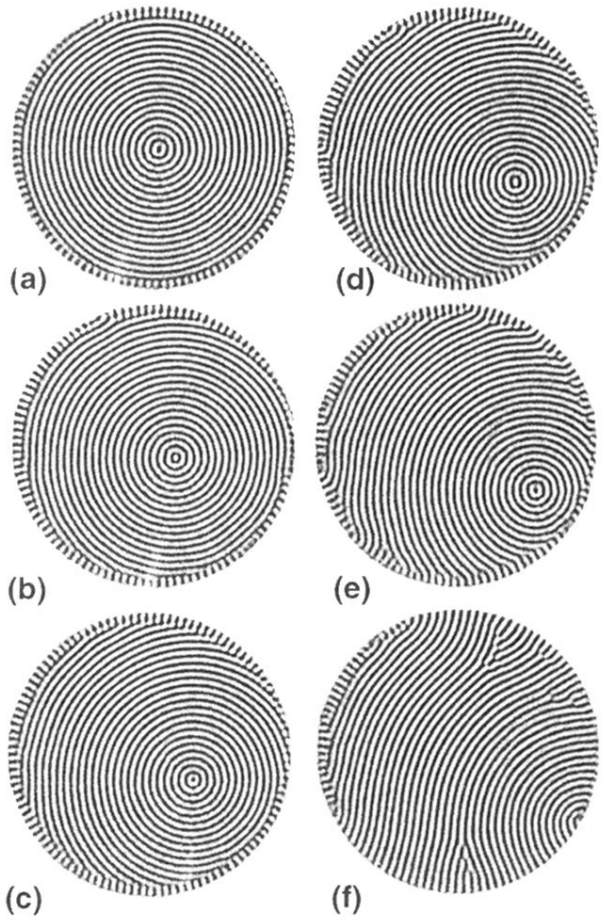

FIG. 15. Destruction of concentric-roll pattern at $\epsilon=0.102$ and for $\Gamma=41$. Elapsed times (arb. orig.) are (a) 0, (b) $5600\tau_v$, (c) $7800\tau_v$, (d) $8520\tau_v$, (e) $9240\tau_v$, (f) $9840\tau_v$.

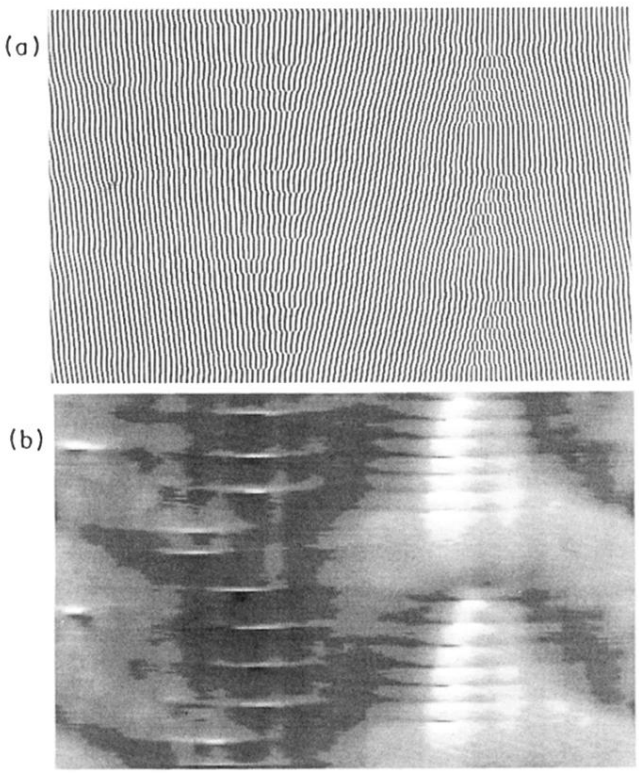

FIG. 17. Space-time plot of cross rolls for $\epsilon=0.099$ and $\Gamma=41$. Time increases in the upward direction, and the images cover $6930\tau_v$. The horizontal axis covers 360°. (a) Shadowgraph intensity of the rolls. (b) Grey-scale-coded wave numbers of the rolls (white: large wave numbers).

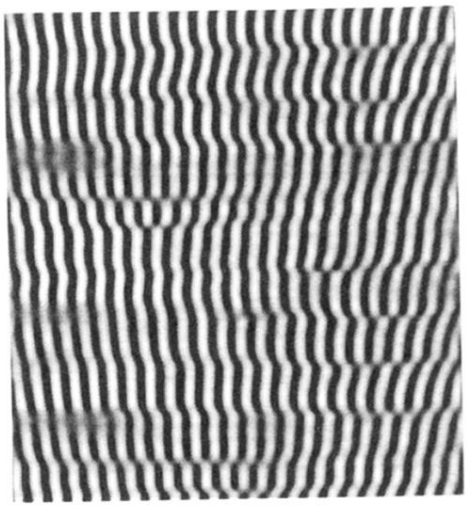

FIG. 18. Enlargement of the source region of Fig. 17(a).

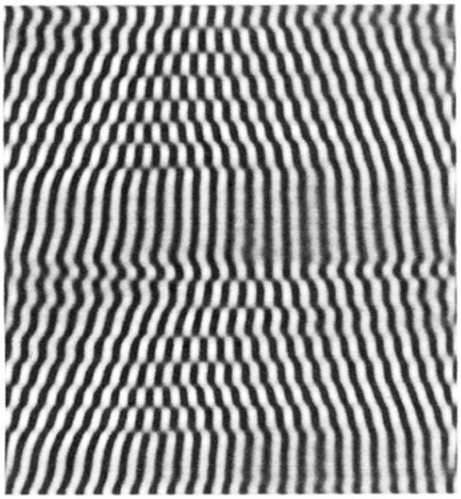

FIG. 19. Enlargement of the sink region of Fig. 17(a).

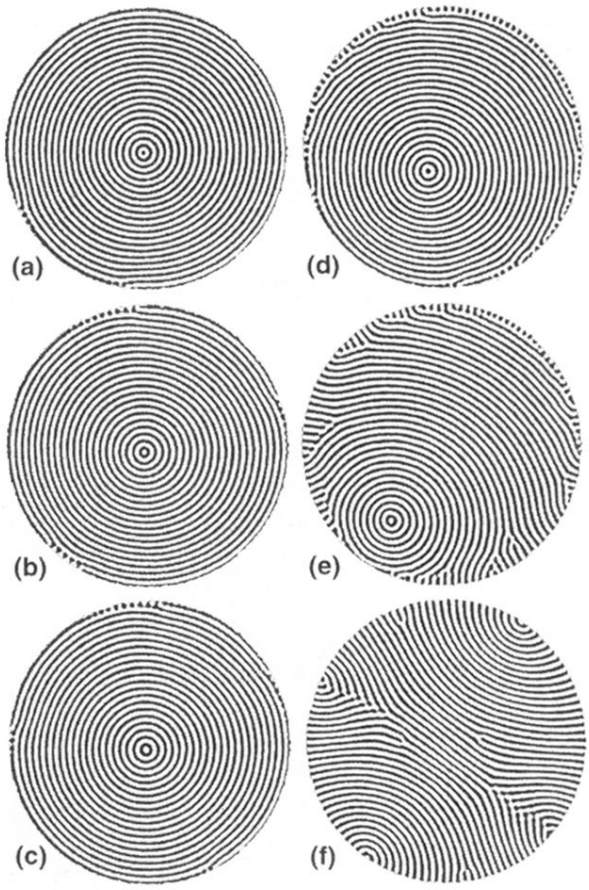

FIG. 21. Destruction of concentric-roll pattern at $\epsilon=0.20$ and for $\Gamma=43$. Elapsed times (arb. orig.) are (a) 0, (b) $1500\tau_v$, (c) $4000\tau_v$, (d) $7600\tau_v$, (e) $9600\tau_v$, (f) $10\,600\tau_v$.

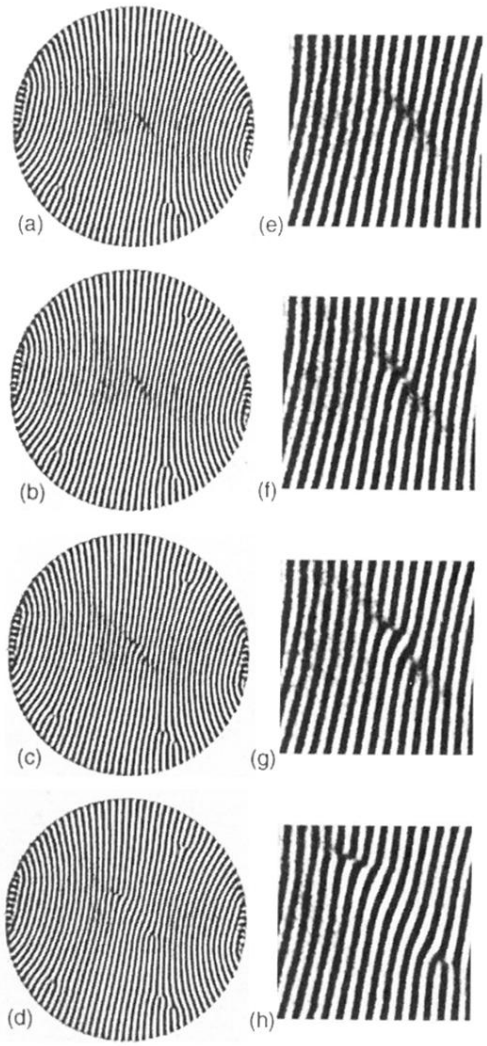

FIG. 22. Defect nucleation mechanism for straight rolls at $\epsilon=0.115$ and for $\Gamma=41$. On the left the entire cell is shown. The right gives a magnified central portion. Elapsed times (arb. orig.) are (a) 0.0, (b) $1.3\tau_v$, (c) $2.6\tau_v$, (d) $9.0\tau_v$, (e) $0.0\tau_v$, (f) $1.3\tau_v$, (g) $2.6\tau_v$, and (h) $9.0\tau_v$.

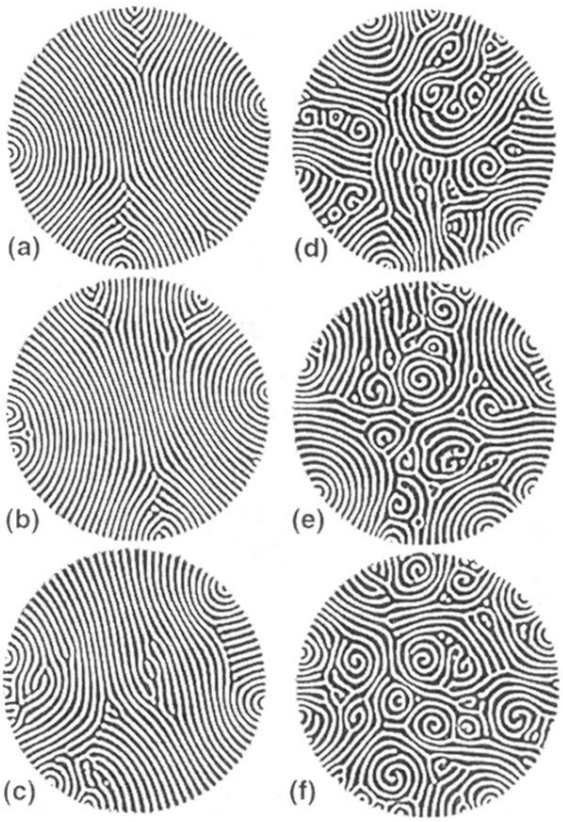

FIG. 23. Typical patterns for $\Gamma = 41$ and $\epsilon =$ (a) 0.34, (b) 0.47, (c) 0.61, (d) 0.75, (e) 0.88, and (f) 0.89.

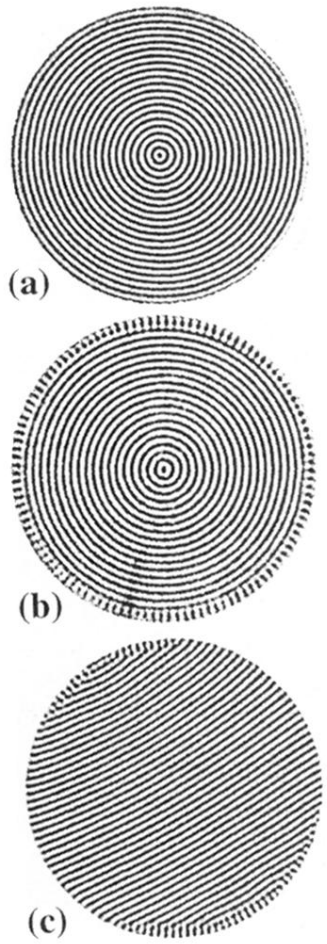

FIG. 3. Patterns at $\epsilon \approx 0.04$. (a) Concentric-roll pattern for $\Gamma = 43$; (b) cencentric-roll pattern for $\Gamma = 41$; (c) straight-roll pattern for $\Gamma = 43$.

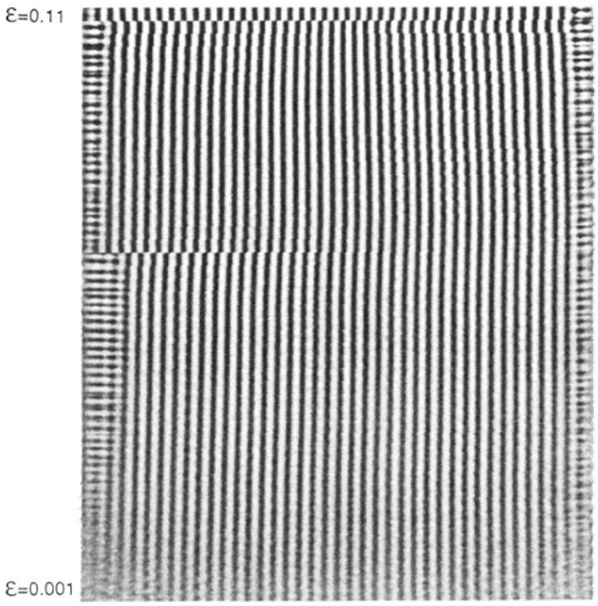

FIG. 5. Composite shadowgraph image showing straight-roll pattern evolution with ϵ for $\Gamma = 41$.

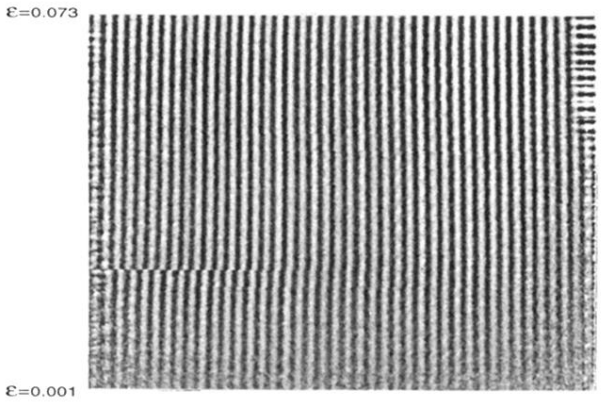

FIG. 6. Composite shadowgraph image showing straight-roll pattern evolution with ϵ for $\Gamma = 43$.